Dose-Free Monitoring of Radiotherapy Treatments With Scattered Photons: First Experimental Results at a 6-MV Linac

Hugo Simões, *Member, IEEE*, Micaela Cunha, Marco Pinto, *Member, IEEE*, Joana Gonçalves, Liliana Sampaio, Ricardo J. Ferreira, Henrique M. Saraiva, Ana Rita Barbeiro, Miguel Capela, Brígida Ferreira, Paulo Fonte, Sharif Ghithan, *Student Member, IEEE*, Antonio Leal Plaza, Maria do Carmo Lopes, Paulo Martins, *Student Member, IEEE*, and Paulo Crespo, *Member, IEEE*

***Abstract*—Radiotherapy (RT) is nowadays, after surgery the most frequently used treatment of cancer. For predicted clinical outcomes it is of importance assuring that the treatment plan is correctly delivered without dose deviations, namely target underdosage and/or organ-at-risk overdosage. For that, a new multipixel imaging technique for real-time dose verification during photon RT has been proposed (RTmon). The principle of operation of RTmon relies on the detection of scattered photons emitted perpendicularly to the beam direction. First scanned, single-pixel experimental results are presented. These results were obtained with a collimated γ-ray detector operated under a 6-MV clinical linac beam. A large contaminating background originating from the head of the linac was found. We show that its mitigation is possible by (1) using appropriate shielding, (2) decreasing the scintillator volume pointing towards out-of-field, background-prone regions, (3) optimizing the collimation by means of detector positioning, and (4) applying background subtraction techniques. Simulation and experimental data show that multiple scattering inside a phantom target constitutes an additional source of background that increases along the beam direction due to momentum conservation in collisions between the incoming photons and target electrons. This second source of background can be reduced effectively by optimizing the distance between the collimated detector and the beam axis, at the expense of decreased collimation sensitivity. Despite the harsh therapeutic irradiation conditions, background and noise suppression by appropriate techniques renders the scanned experimental results quite similar to the dose obtained by means of Geant4 simulations. Such experimental results suggest that this detection system may be useful for non-invasive, real-time, *in-situ* dose verification in external X-ray beam radiotherapy.**

***Index Terms*—Dose monitoring, medical imaging, Monte Carlo simulation, photon collimation, radiation therapy.**

Manuscript received May 31, 2012; revised February 22, 2013; accepted May 23, 2013. Date of publication July 01, 2013; date of current version August 14, 2013.

H. Simões was supported in part by an INOV.C grant co-funded by QREN, under the Mais Centro Program and the European Regional Development Fund. P. Crespo (SFRH/BPD/39223/2007), P. Martins (SFRH/BD/45040/2008), and S. Ghithan (SFRH/BD/51139/2010) were supported by FCT – Fundação para a Ciência e a Tecnologia, Lisbon, and A. R. Barbeiro was supported by a Leonardo da Vinci scholarship from the High Institute for Allied Health Technologies from Polytechnic of Porto, Portugal.

H. Simões is with LIP – Laboratório de Instrumentação e Física Experimental de Partículas, University of Coimbra, 3004-516 Coimbra, Portugal (e-mail: hugo.simoes@coimbra.lip.pt).

M. Cunha and M. Pinto were with LIP-Laboratório de Instrumentação e Física Experimental de Partículas, University of Coimbra, 3004-516 Coimbra, Portugal. They are now with the Institut de Physique Nucléaire de Lyon, 69622 Villeurbanne Cedex, France (e-mail: micaela.cunha@coimbra.lip.pt; marco.pinto@coimbra.lip.pt).

J. Gonçalves, L. Sampaio, R. J. Ferreira, and H. M. Saraiva were with LIP-Laboratório de Instrumentação e Física Experimental de Partículas, University of Coimbra, 3004-516 Coimbra, Portugal and also with ISEC-Instituto Superior de Engenharia de Coimbra, 3030-199 Coimbra, Portugal (e-mail: tog_api@hotmail.com; lilianasampaio_1@hotmail.com; ricferreira23@gmail.com; hmsaraiva90@gmail.com).

A. R. Barbeiro and A. Leal Plaza are with Facultad de Medicina, Universidad de Sevilla, 41009 Sevilla, Spain (e-mail: arpereira@us.es; alplaza@us.es).

M. Capela and M. C. Lopes are with Instituto Português de Oncologia de Coimbra Francisco Gentil, E.P.E., 3000-075 Coimbra, Portugal (e-mail: montouro@ipocoimbra.min-saude.pt; mclopes@ipocoimbra.min-saude.pt).

B. Ferreira is with I3N – Institute of Nanostructures, Nanomodelling and Nanofabrication, Departamento de Física, Universidade de Aveiro, 3810-193 Aveiro, Portugal (e-mail: brigida@ua.pt).

P. Fonte is with LIP – Laboratório de Instrumentação e Física Experimental de Partículas, University of Coimbra, 3004-516 Coimbra, Portugal, and also with ISEC – Instituto Superior de Engenharia de Coimbra, 3030-199 Coimbra, Portugal (e-mail: fonte@coimbra.lip.pt).

S. Ghithan, P. Martins, and P. Crespo are with LIP – Laboratório de Instrumentação e Física Experimental de Partículas, University of Coimbra, 3004-516 Coimbra, Portugal, and also with the Physics Department, Faculdade de Ciências e Tecnologia, University of Coimbra , 3004-516 Coimbra, Portugal (e-mail: sharif.ghithan@coimbra.lip.pt; pmartins@coimbra.lip.pt; crespo@lip.pt).

Color versions of one or more of the figures in this paper are available online at http://ieeexplore.ieee.org.

Digital Object Identifier 10.1109/TNS.2013.2265137

I. Introduction

THE main goal of radiotherapy (RT) is to guarantee maximum dose delivered to the tumor, while maintaining minimum healthy-tissue dosage to limit undesirable side-effects. Modern RT monitoring systems seeking the detection of morphological changes are utilized in image guided radiation therapy (IGRT). IGRT has its own advantages, limitations, and possible side effects, namely an increased dosage due to successive, repetitive computerized mega/kilovoltage imaging [1], [2]. Within IGRT limitations, one of particular significance is its inability to respond with absolute sensitivity and specificity to the needs of RT monitoring. Our groups introduced a new imaging technique that shows potential for dose verification in external beam radiotherapy [3], which can provide useful information to complement IGRT. This technique is based on orthogonal ray imaging, i.e., detection of photons escaping a patient -being irradiated- at right angles with the beam direction. The system under development is capable of monitoring RT sessions in real time by means of a dedicated, gamma-camera-like photon detection system [3]. This detection system must acquire data during RT treatments, selecting Compton-scattered or bremsstrahlung photons arising from the

target (patient). These photons are spatially correlated with the physical dose. Additionally, the system must reject events that are not spatially correlated with the prescribed dose by using optimized collimation, energy windowing, and appropriate noise and background reduction techniques. In this work, the proof-of-concept of such system is verified experimentally in a radiotherapy environment.

A. Rationale for (Real-Time) Radiotherapy Monitoring

The greatest challenge for RT or any other cancer therapy is to attain the highest probability of cure with the least morbidity [4]. In RT treatments, it is desirable to deliver a maximum dose to the tumor while healthy tissues and organs at risk (OAR) are exposed to minimal dose. In single-fraction as well as in fractionated treatment courses, patient misalignments and anatomical changes can occur between sessions or in the time frame occurring between the treatment plan and the actual treatment, leading to the possibility of target underdosage or OAR overdosage. Even in devices with rigid fixation, positioning errors higher than 10 mm may occur [2]. Some examples of internal anatomical changes are the presence of edema (if close to the target tumor underdosage may be induced), tumor regression during the treatment (may result in overdosage of surrounding OAR), and tumor progression (potential tumor underdosage) [5]. The filling of empty cavities due to inflammation and the increase of permeability in irradiated tissues also represent responsive biological mechanisms to the RT injury [6].

B. Detector Concept for (Real-Time) Radiotherapy Monitoring

The goal of this detection system [3] is to provide real-time monitoring of RT treatments, potentially allowing for dose verification. Its implementation in a radiotherapy environment is shown in Fig. 1 [3]. The system, called RTmon, consists of a single, or multiple, detector-head(s) positioned at right-angle(s) with the beam direction. A high-energy collimator is positioned in front of the gamma-ray detector. Thus only the photons that are scattered from the target (i.e., patient) and emitted perpendicularly to the beam direction are collected by the detector. By correlating each detected event with the beam's incoming position, it is possible to project the 2D information given by each detection system into the 3D image space of the patient without any additional reconstruction requirements. This 2D image information may be further used to allow for a real-time image to be constructed as the beam is being delivered. A simulation example of the aforementioned principle of operation of RTmon is shown in [7] in the field of intensity modulated radiation therapy (IMRT). That study describes how one or more so-called photon beamlets irradiating a tumor in the head of an anthropomorphic phantom may be monitored in real time by means of one or more RTmon detector systems such as the one being described in this work.

Fig. 2 presents results obtained by means of Geant4 [8], [9] simulations where a fully collimated RTmon system was evaluated by Monte Carlo [3]. A multihole collimator (Fig. 2, top left) made of lead was constructed in Geant4. Its dimensions were a front face with $300\ \mathrm{mm} \times 150\ \mathrm{mm}$, and a thickness of 182.93 mm. Hexagonal holes were implemented in it in order to collimate photons with energies of the order of 600 keV.

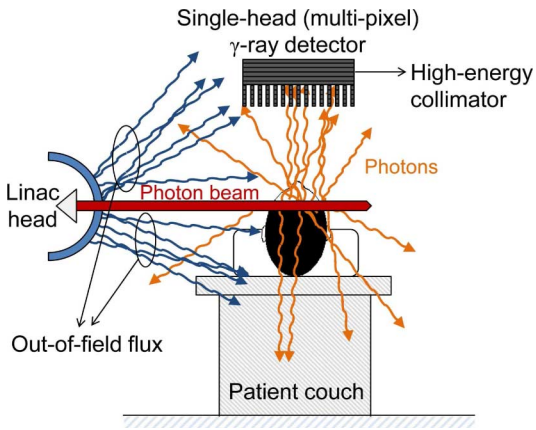

Fig. 1. Side view of the RTmon detector concept.

The face-to-face distance of each hole and the septa thicknesses were, respectively, 2.7080 mm and 0.91566 mm. A rectangular perfect detector also covering $300\ \mathrm{mm} \times 150\ \mathrm{mm}$ was positioned behind the collimator. At this stage, each event hitting this perfect detector was considered as true. The simulated phantom shown in Fig. 2, top right, was irradiated by a 6– MV circular photon beam with 30– mm diameter. The phantom consisted of a water cylinder with 180– mm diameter and 300– mm length. Near to its center, an air cavity and an insert of bone were introduced. The distance between the front face of the collimator and the phantom surface was 190 mm. The middle plot in Fig. 2 shows the 2D distribution of events that crossed the multihole collimator and reached the perfect detector. The bottom plot in the same figure shows the simulated depth-dose profile (red, dashed line) and the corresponding profile of scattered photons (blue, solid line) detected after the multihole collimator. The scattered photon profile was obtained by integrating the 2D distribution in the X direction. The integration was limited to $-15\ \mathrm{mm} \leq X \leq 15\ \mathrm{mm}$ since that is the width of the penetrating photon beam. The visual similarity between simulation and dose profiles, quantified in [3], highlights the intrinsic potential of RTmon.

Finally, it must be stated that due to momentum conservation in their collisions with atomic electrons, some scattered photons are projected in the forward direction [3]. This effect is evident in the profiles of Fig. 2 bottom, where a discrepancy exists at low depths ($Z \leq -80\ \mathrm{mm}$) between the profile of collected photons and the depth-dose profile. This discrepancy depends of factors such as (1) the aperture of the collimator holes, (2) the distance between the photon detector and the penetrating beam, and (3) the distance between the photon detector and the outer surface of the target being irradiated. Nevertheless, optimizing these different distances lies outside the scope of the present work, which focuses on providing first experimental evidence that RTmon profiles may be correlated to some point with the depth-dose profile.

II. Materials and Methods

A. Experimental Setup and Optimization of Photon Acceptance

The multihole collimator setup shown in Fig. 2 (top left) was first optimized by means of Monte Carlo simulation with Geant4

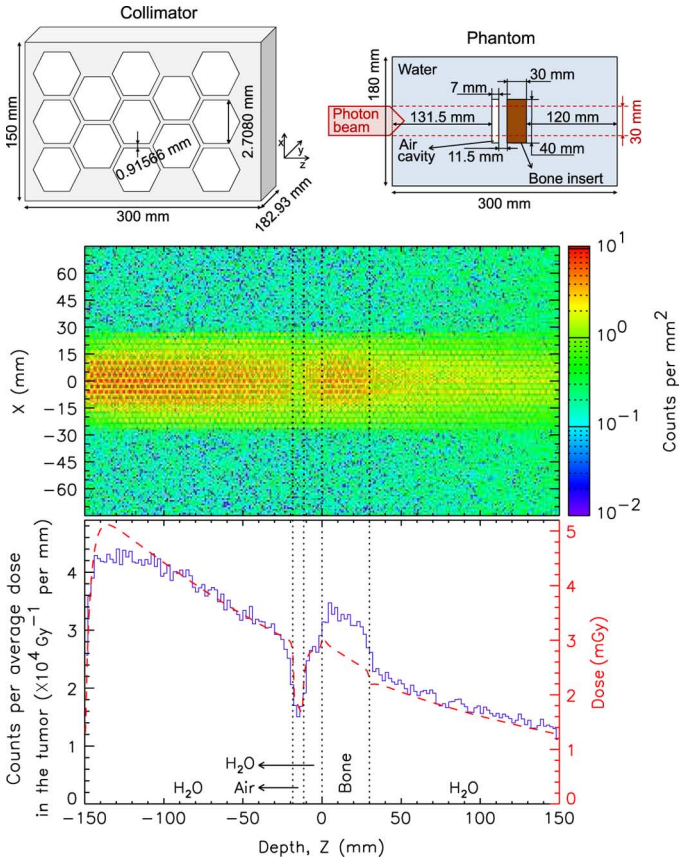

Fig. 2. *Top left:* Scheme of the collimator implemented in Geant4. Its parameters were manipulated in order to collimate photons with energies of the order of 600 keV [3]. *Top right:* Schematic view of the simulated phantom used to obtain the profiles in the middle and bottom plots. *Middle and bottom:* Results obtained by means of Geant4 simulation with a multipixel, fully-collimated system. The *middle* image shows the 2D distribution of photon counts collected during irradiation, whereas in the *bottom* image the corresponding depth-dose profile (red, dashed line) is plotted along with the profile of detected photons (blue, solid line).

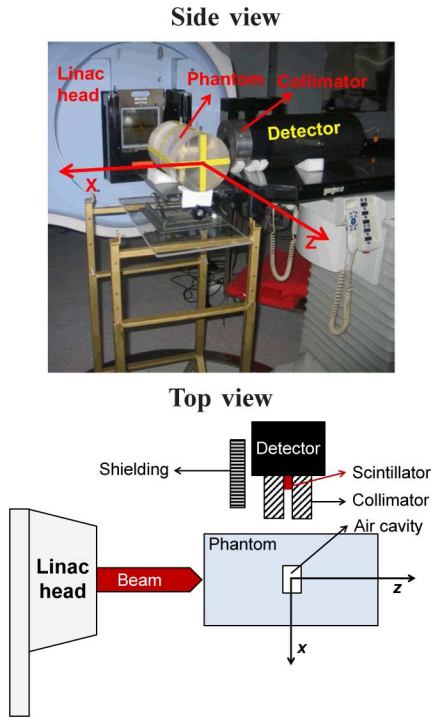

Fig. 3. Experimental setup. *Top*: Photograph of the experimental setup at the irradiation site. *Bottom*: Scheme of the top view of the experimental setup.

[3]. The configuration yielding the best results, described in section Section III-A, allowed for parameters such as optimum collimator height and diameter of the collimator hole to be known. These were then implemented on a single-pixel detector that was constructed in order to obtain the first in-beam results presented in this work.

Fig. 3 shows the single-pixel setup implemented for the in-beam longitudinal scanning experiments described in the next sections. An iron-Cerrobend™ collimator with 149–mm height and an inner-hole with 6–mm diameter was positioned perpendicular to the beam axis, at a distance of 110 mm from a 180–mm diameter polymethylmethacrylate (PMMA) phantom (i.e., at 200 mm from the central beam axis). Four crystals of cerium-doped lutetium yttrium oxyorthosilicate (LYSO:Ce), each with a length of 20 mm and a front face of $2\ \mathrm{mm} \times 2\ \mathrm{mm}$, were coupled together and used as scintillator crystal for X-ray conversion. The four crystals were wrapped together in Teflon tape thus forming a single crystal with $4\ \mathrm{mm} \times 4\ \mathrm{mm}$ front face. This assembly was inserted into the collimator hole, with its outer face being coupled with silicon oil to the photocathode of a photomultiplier tube (PMT). The PMT was further protected from radiation by means of a hollow, iron cylinder with a wall thickness of 20 mm, as shown in the photograph in Fig. 3. With these dimensions, this detection system is able to collect photons scattered in the target center with an acceptance angle θ in the range $88.7\ ^\circ \leq \theta \leq 91.3\ ^\circ$. Such collimator does not correspond to the optimized dimensions obtained from the Monte Carlo simulations [3]. Nevertheless, it allowed for the first tests to be performed and presented in the next sections.

The aforementioned PMMA target has a density of $1.19 \pm 0.1\ \mathrm{g/cm^{-3}}$. In its center, the phantom has an air cavity with 20– mm length and 30–mm diameter (Fig. 3). All experiments described in the next sections were performed in a radiotherapy environment by using a clinical X-ray beam with a field size of $30\ \mathrm{mm} \times 30\ \mathrm{mm}$ at the isocenter, delivered by a Siemens ONCOR Avant-Garde linac operated at 6 MV and installed at the Center of Oncology of Coimbra (IPOCFG, E.P.E.).

B. Data Acquisition and Processing

1) Linac Beam Macrostructure: The linac macrostructure was analyzed by acquiring events coming from the linac head (without a phantom in front of the detector). The beam pulse has a period of $\sim 4.7\ \mathrm{ms}$, corresponding to a macrostructure operation frequency of $\sim 213\ \mathrm{Hz}$.

2) Unformatted Versus Formatted Signal Shape: A PMT fed with a negative voltage was used for detecting the scintillation light from the LYSO crystal. The acquisition was performed with a free running oscilloscope sampling at approximately 2 MHz and with ca 5% dead time. The fast decay constant of LYSO (41 ns) results in single events returning to baseline in about 120 ns. Hence, it was necessary to shape the PMT signal output before data sampling in order to allow for enough waveform samplings points to be collected per event. Fig. 4 outlines

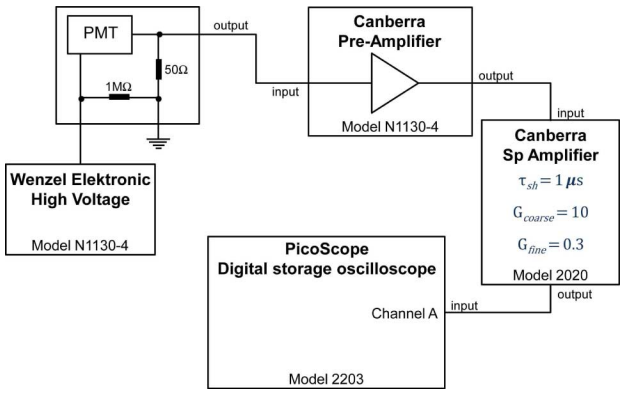

Fig. 4. Scheme of the readout electronics utilized in the experiments.

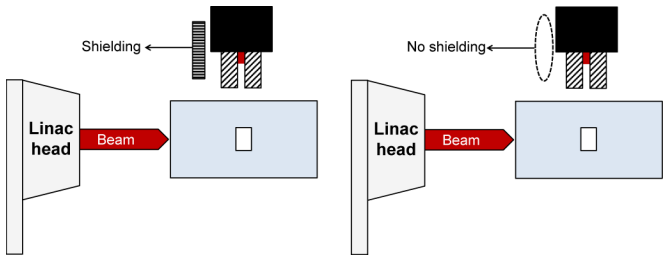

Fig. 5. Experimental setup used to analyse the influence of Cerrobend™ shielding.

the detector bias, electronics shaping, and readout chain implemented. The PMT output feeds a pre-amplifier (Canberra model 2005), followed by a spectroscopy amplifier (Canberra model 2020) with output connected to a self-programmed, linux-controlled oscilloscope (PicoScope model 2203). It must be stated that the light being read from the LYSO scintillator corresponds to X-rays piled up in the macrostructure of the linac beam delivery. In fact, the high voltage feeding the PMT had to be lowered from the typical -900 V necessary to see a pulse from a radioactive source in the laboratory, down to ca -465 V so that no pulse saturation would occur when reading at IPOCFG, E.P.E. In summary, results correspond to pulse height spectra of events collected during the macropulses of the linac.

3) Signal Sampling and Restoration: With the signal formatting implemented (Fig. 4), the data acquisition (DAQ) system was able to collect at least eight samples per pulse Section III-B2. However, the 8-bit resolution of the oscilloscope posed another technological challenge. When the maximum amplitude of each pulse event was used, the spectrum obtained had a very poor resolution. To overcome this problem, each detected waveform was instead fit to a Gaussian function, and the peak of the fit was used. All this processing was performed with self-developed GNU Octave [10] functions.

C. Out-of-Field Linac Background Flux

1) Quantification: It is a well known fact that there is a background flux of photons and other particles escaping from the linac head. Investigation of the impact of such an out-of-field flux on the development of secondary malignancies is ongoing (e.g., [11]). Different types of accelerators produce different out-of-field doses due to their different shielding designs [12].

This background flux escaping from the head of the linac poses some technological problems for RTmon. When this out-of-field flux penetrates the RTmon detector, the signal amplitude increases beyond saturation if no countermeasures are taken. Furthermore, this background reduces significantly the signal-to-noise ratio at the detector level jeopardizing the detection of the signal of interest arising from radiation scattered in the target. Although it is difficult to completely remove such background signal, it was mitigated by (1) introducing Cerrobend™ shielding between the detector and the head of the linac, (2) optimizing the geometrical orientation of the detector, and (3) implementing a background suppression readout approach.

In order to quantify such background particle flux, the EGSnrc Monte Carlo code [13] was used. A total of 5×10^8 particles was simulated to arrived at a plane perpendicular to the beam direction, with such plane positioned at the isocenter (i.e., at 1000 mm distance from the electron target for bremsstrahlung production). A field of 30 mm$\times$ 30 mm was defined at the isocenter, irradiated with a 6– MV photon beam. The linac head simulated corresponds to the Siemens PRIMUS treatment head installed at the Hospital Universitario Virgen Macarena, in Seville.

2) Mitigation by Means of Shielding: The influence of Cerrobend™ shielding between the linac head and the detector was evaluated. A block of Cerrobend™ with 60–mm thickness was used as shielding. Fig. 5 shows the experimental setup. The phantom was left in the position of irradiation to make sure that the signal variation in the detector was only due to the shielding conditions. The measurements consisted in acquiring a pulse height spectrum with the shielding Cerrobend™ positioned between the linac and the detector (Fig. 5, left), and a second pulse height spectrum obtained without Cerrobend™ shielding (Fig. 5, right).

D. Scanning Along the Phantom

1) $\mathrm{Signal} + \mathrm{Background}$*:* In order to make a longitudinal scan (Z-axis), the detector was moved in respect to the phantom from a proximal position of $Z = -120$ mm to a distal position of $Z = +120$ mm with incremental steps of 20 mm. The pulse height spectrum with the Gaussian amplitude of each event was computed for every event in all positions. The resulting pulse height spectra obtained were fit to a Gaussian distribution. Each mean value obtained was plotted along the Z axis.

2) Background Only: The procedure described in the previous subsection was repeated, now with a change in the experimental setup: a tungsten block was placed in front of the inner hole of the iron-Cerrobend™ collimator. In this way the detector is not directly exposed to radiation from the phantom, i.e., the radiation scattered in the phantom that reaches the detector is highly suppressed. Consequently, this measurement samples mainly background radiation (so-called *dummy measurement*).

3) Background Subtraction: Each measured *background* (Section II-D2) pulse height spectrum was subtracted from the $signal + background$ pulse height spectrum (Section II-D1)

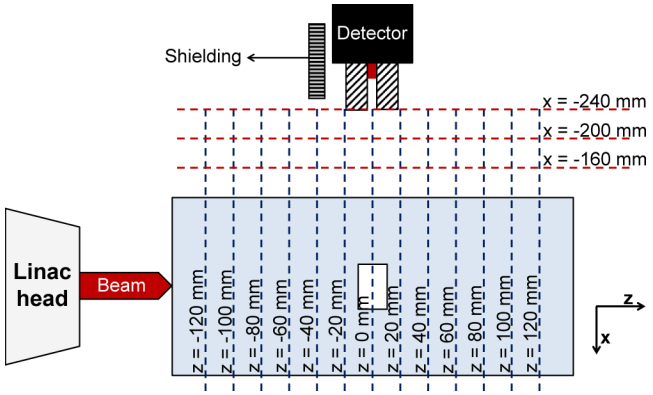

Fig. 6. Scheme of the phantom longitudinal scan (depth scan: along Z-axis with measurements performed at each vertical, blue-dashed line); and transaxial scan (at different X distances between the beam axis and the collimator front face: horizontal, red-dashed lines).

to determine a background-free pulse height spectrum that was also plotted along the Z-axis.

4) Optimization of Detector/Phantom Separation: A scan similar to that described above was made in the X direction (perpendicular to the beam axis, Fig. 6), with 40–mm steps ($X = -160$ mm corresponds to a distance of 70 mm from the surface of the phantom).

E. Validation of Geant4 Photon Profiles

In order to validate the capability of the simulation code to reproduce the single-pixel experimental results, some simulations were performed using the Geant4 toolkit [8], [9], version 9.4, and the emstandard_opt3 physics list (only electromagnetic processes were activated). A 6– MV spectrum from a linac from Varian Medical Systems, adapted from [14] into [3], was used. The physics list implemented was validated in [3]. A comparison between simulated data and measured data published in [15], allows for a large degree of confidence in the simulation results [3]. A setup similar to the one described in section Section II-D1 composed by a PMMA phantom and a single-pixel photon detection system (i.e., a perfect detector placed beyond an iron-Cerrobend™ collimator) was implemented, and the procedure described in section Section II-D was simulated by varying the Z distance and having the distance X fixed to $X = -200$mm.

III. Experimental Results

A. Experimental Setup and Optimization of Photon Acceptance

Fig. 7 shows that the collimator design significantly affects how closely the RTmon can measure the dose profile. The coarse collimator allows measurement of photons scattered in the forward direction in addition to those scattered at 90 degrees, while the fine collimator does not allow these unwanted events to reach the detector. The term *coarse collimation* corresponds to a multihole collimator with a wall height of 116.99 mm, a hexagonal hole with a face-to-face distance of 2.0196 mm, and a septa thickness of 0.52669 mm [3]. The term *fine collimation*, on the other hand, is achieved with a wall height of 182.93 mm, a hole face-to-face distance of 2.7080 mm, and a septa thickness of

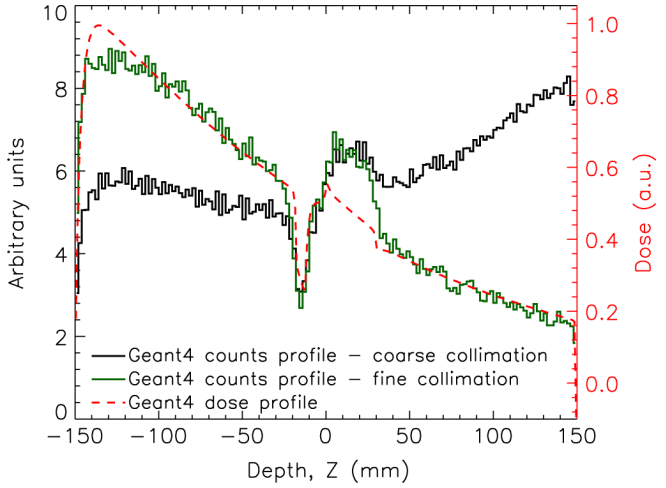

Fig. 7. Simulated (geant4) photon count profiles with a less favorable coarse collimation (black profile) versus profiles obtained with a finer collimation (green profile). only proper fine collimation shows a good correlation with the depth-dose profile (red, dashed line).

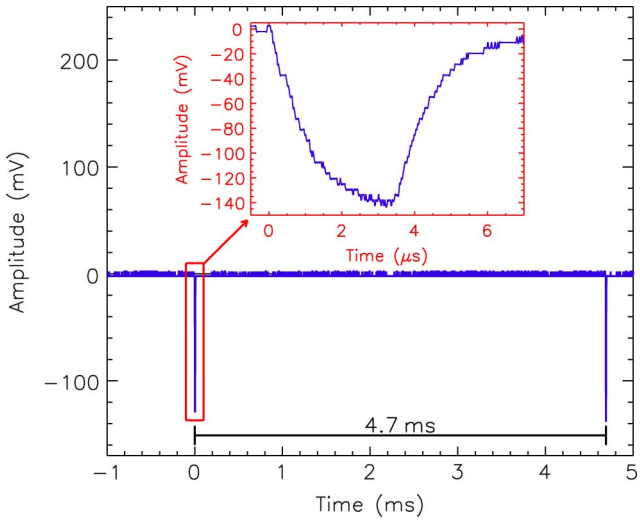

Fig. 8. Macrostructure of the linac beam measured with a single-pixel collimated detector.

0.91566 mm. In both cases, the distance between the front face of the collimator and the beam central axis was 280 mm, for the phantom shown in Fig. 2 (top right).

B. Data Acquisition and Processing

1) Linac Beam Macrostructure: The inset in Fig. 8 shows that the pulse collected during a single linac macropulse, which lasts approximately 6.5 μs, has a rise time slightly less than 3 μs. Due to hardware bandwidth limitations we cannot infer information about the microstructure of the linac beam.

2) Unformatted Versus Formatted Signal Shape: Fig. 9 highlights both the signal acquired directly from the PMT (top) and after the signal processing electronics were implemented (bottom). The red arrows represent the sampling times in free-running mode.

3) Signal Sampling and Restoration: Fig. 10 shows a sampled waveform (diamonds) and the respective Gaussian fit (dashed line).

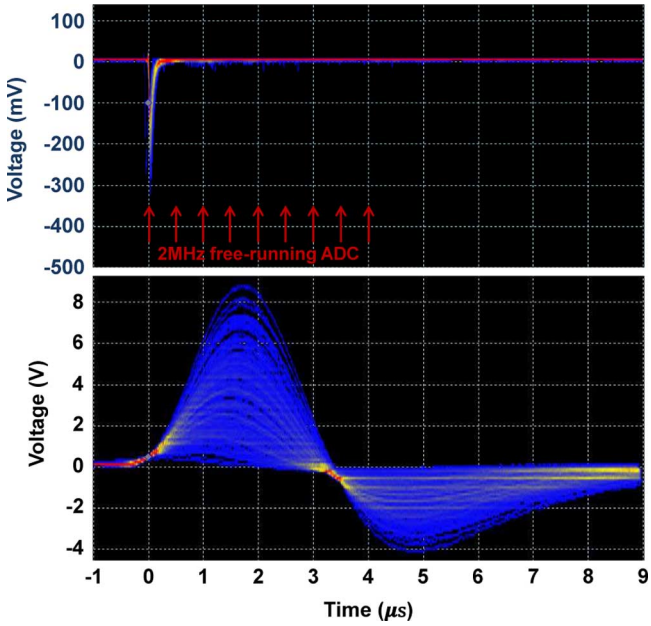

Fig. 9. Persistence display showing signals acquired directly at the PMT *(top)*, and after signal shaping *(bottom)*, the latter having at least eight samples collected per waveform. Red arrows represent sampling times at 2 MHz sampling rate.

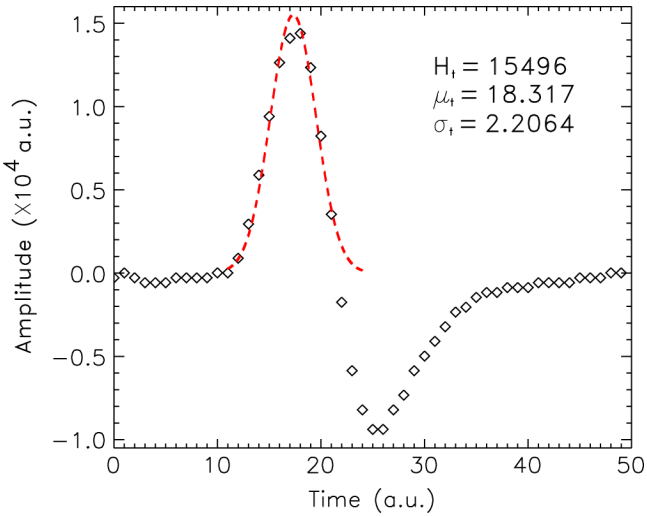

Fig. 10. Sampled waveform (diamonds) and corresponding Gaussian fit (dashed line).

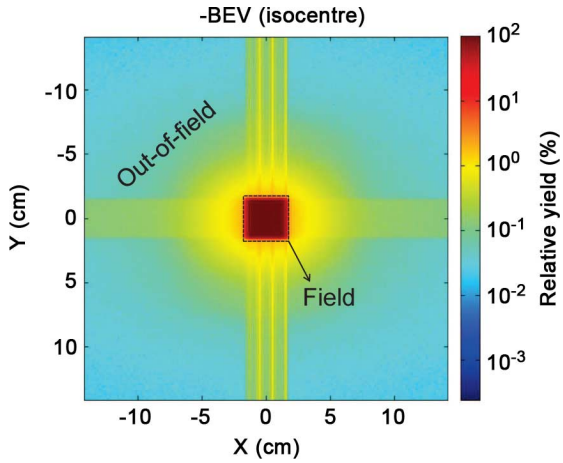

Fig. 11. Beam's eye view (bev) of the simulated particle flux arriving at the isocenter of a $30\ \mathrm{mm} \times 30\ \mathrm{mm}$ field (100% relative flux) together with relative out-of-field radiation.

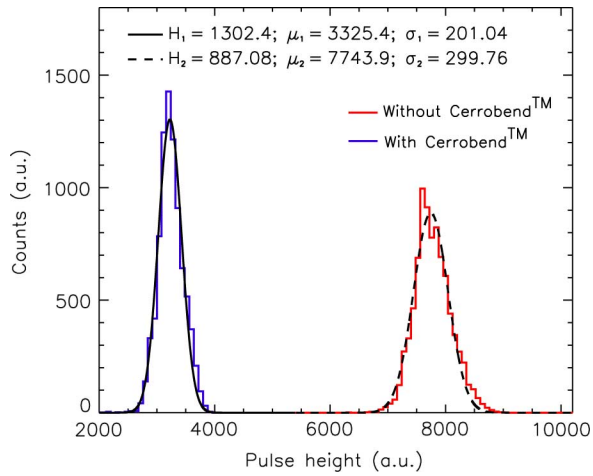

Fig. 12. Pulse height spectra obtained with (left, blue) and without (right, red) shielding between the linac head and the detector. A 60-mm-thick Cerrobend™ block was used for shielding. The phantom was irradiated at the isocenter. The black, dashed and solid lines represent the respective Gaussian fits.

C. Out-of-Field Linac Background Flux

1) Quantification: Fig. 11 quantifies the out-of-field percentage flux arriving at the plan at the isocenter (a total of 1.05×10^8 particles out of 5×10^8 initial histories).

The irradiation field detailed in section Section II-C1 was defined with the multileaf collimator and collimating jaws in the Y and X directions, respectively, which can be noticed in Fig. 11 by the visible effect of the inter- and intra leaf transmission.

2) Mitigation by Means of Shielding: As previously mentioned, the out-of-field flux escaping the linac head can be partly reduced by utilizing proper shielding material. By using a 60-mm-thick Cerrobend™ block, a background reduction η of 57% was achieved (Fig. 12):

$$\eta = \frac{\mu_2 - \mu_1}{\mu_2} \times 100. \tag{1}$$

D. Scanning Along the Phantom

1) Signal + Background: Fig. 13 compares the pulse height spectra obtained with (left, blue) and without (right, red) the tungsten block positioned in front of the collimator (i.e., *background only* and *signal+background*, respectively) for a detector setup located at a proximal position of $Z = -120\ \mathrm{mm}$. In both cases the Cerrobend™ shielding block was positioned between the linac head and the detector, and the phantom was located in the irradiation position. The pulse height spectra show a larger signal present only when the detector was exposed

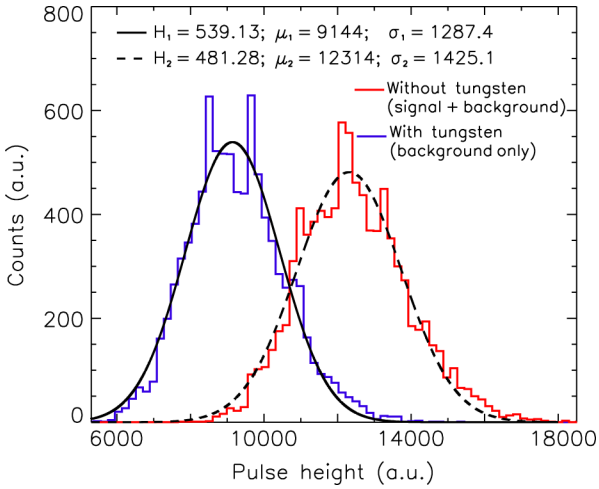

Fig. 13. Pulse height spectra obtained with tungsten block (blue histogram, left) and without tungsten block (red histogram, right) in front of the hole of the collimator, with the detector setup positioned at a proximal position with $Z = -120$ mm. The black solid and dashed lines show the Gaussian fits obtained for each spectrum.

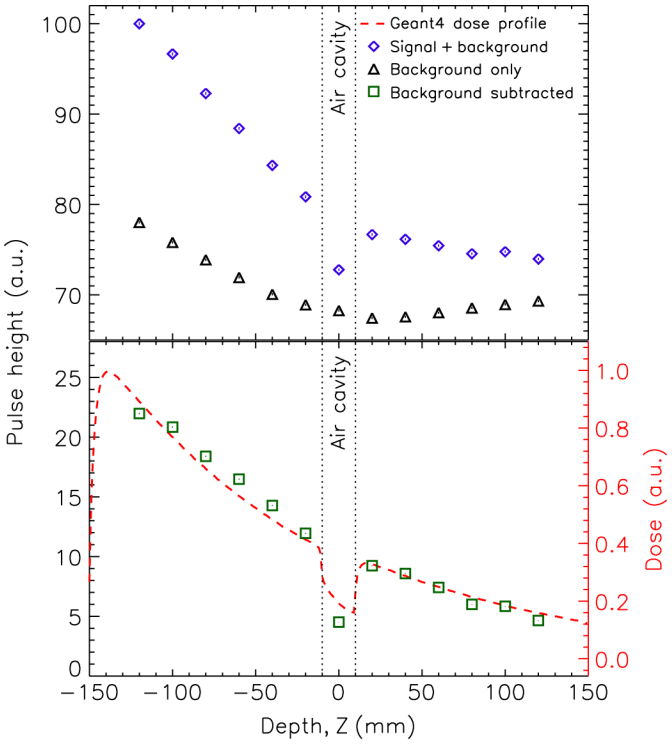

Fig. 14. Scan profiles along the phantom depth Z, with the distance X fixed to $X = -200$ mm. Open diamonds (blue) correspond to $signal + background$, open triangles (black) show the *background signal*, and open squares (green) are related to the *background subtracted signal*. The red dashed line is the Geant4-simulated depth-dose profile.

to the phantom (i.e., without tungsten blockage), therefore allowing the physical signal arising from the phantom to reach the detector.

2) Backgroundonly: The pulse height spectrum obtained with the tungsten block in front of the collimator was already presented and discussed in the previous section.

3) Background Subtraction: Fig. 14 shows the results of one depth scan along the longitudinal direction, i.e., Z-axis,

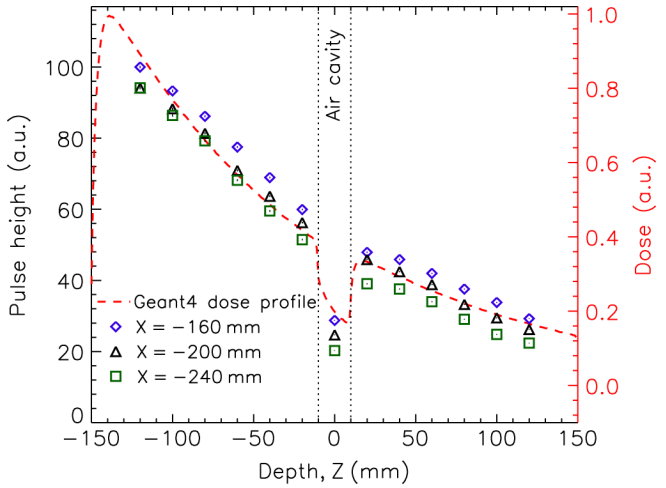

Fig. 15. Depth-profiles obtained by scanning the detector along the phantom (Z-axis) at different X distances from the isocenter. Diamonds (blue), triangles (black) and squares (green) correspond to the depth profiles acquired at positions $X = -160$ mm, $X = -200$ mm and $X = -240$ mm, respectively. The red dashed line represents the Geant4-simulated depth-dose profile.

with X fixed to $X = -200$ mm. Open diamonds (blue) correspond to $signal + background$, open triangles (black) show the *background signal*, and open squares (green) are related to the *background subtracted signal*. The red dashed line is the Geant4-simulated depth-dose profile (with beam divergence taken into account). All data points were normalized relative to the highest value (proximal position at $Z = -120$ mm, corresponding to the setup $signal + background$). All error bars fall within the size of their corresponding data symbols, as can be confirmed by their values: errors obtained for the $signal + background$, *background signal*, and the *differential signal* were 0.165%, 0.171%, and 0.233%, respectively. The dose profile is plotted in arbitrary units and was visually adjusted to the background subtracted profile.

4) Optimization of Detector/Phantom Separation: Results for depth-scans along the phantom (beam direction) at different distances from the phantom (X-axis) are presented in Fig. 15. Diamonds (blue), triangles (black), and squares (green) correspond to the depth profiles acquired at positions $X = -160$ mm, $X = -200$ mm, and $X = -240$ mm, respectively; the red dashed line again represents the Geant4-simulated depth-dose profile. All data points were normalized relative to the maximum experimental height, occurring at the proximal position with $Z = -120$ mm and $X = -160$ mm. Error bars are smaller than the size of the data symbols with, for example, errors obtained for X positions -160 mm, -200 mm, and -240 mm being 0.348%, 0.365% and 0.396%, respectively.

As can be seen in [3], the diameter of the collimator hole plays a major role in rejecting unwanted events that scatter in the phantom, out of the dose field. Before attempting these measurements, coarse Geant4 simulations were carried out that pointed to optimum distances being within those presented in Fig. 15. The reason why one particular X distance yields the best agreement ($X = -200$ mm) lies in two competing physical effects: smaller X suffers from larger contamination from the linac out-of-field radiation, while larger X suffers from higher

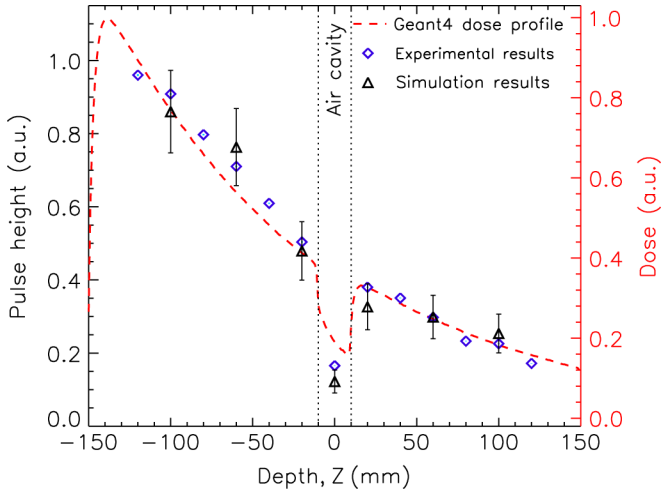

Fig. 16. Experimental (open diamonds, blue) versus simulation results (open triangles, black). The red dashed line corresponds to the Geant4-simulated depth-dose profile.

contamination from unwanted events scattered in the phantom, out of the dose field.

E. Validation of Geant4 Photon Profiles

In Fig. 16 the agreement between the simulated (black open triangles) and the experimental scan (blue open diamonds) obtained at $X = -200$ mm is shown, together with the simulated dose (red, dashed line). There is a good visual correlation between the yields obtained experimentally and by simulation. The error bars for the measured profile are smaller than the size of the data symbols (0.365%).

IV. Discussion

Regarding the optimization of photon acceptance, we have shown that it is important to chose an appropriate geometry for the RTmon collimator. In Fig. 7 the curve labeled *coarse collimation* shows that a too-wide collimation, potentially preferred for providing increased sensitivity, does not suffice in rejecting target-scattered photons that are emitted preferentially in the forward direction due to momentum conservation. A narrower collimation (curve labeled *fine collimation*) was indeed among the fundamental characteristics that allowed obtaining the results presented in this work.

In what concerns the data acquisition and processing strategy implemented, we have proven that the background suppression technique applied becomes useful in order to highlight the physical signal coming from the phantom. In fact, the correlation between the background-subtracted profile and the simulated dose profile along the phantom (Fig. 16) was computed to be 0.9911. This correlation gives a strong evidence of the capability of the proposed system to be used in radiotherapy environments, strongly enhancing the information provided by current IGRT technologies if a similar 2D system may be brought into clinical operation.

A harsh, out-of-field particle flux escaping the linac head was seen to exist. Its magnitude was computed by means of Monte Carlo simulations (Fig. 11). This large flux has implications on detector performance and on the obtainable results. However, its effect was minimized threefold: (1) by means of appropriate shielding, (2) optimized geometry of the gamma-ray detector, that must be oriented preferentially towards the aimed target, and (3) by means of the aforementioned technique for background subtraction. In respect to detector shielding, a background reduction of 57% was accomplished by using a 60-mm-thick Cerrobend™ block positioned between the head of the linac and the detector. Finally, the pulse height spectra obtained with and without a tungsten block obstructing the collimator hole (Fig. 13) clearly demonstrate a larger signal amplitude to be present only when the detector is exposed to phantom-incoming radiation.

V. Conclusions

The experimental results obtained for the RTmon concept being presented here substantiate its potential use not only for monitoring RT treatments in real time, without additional dose to the patient, but also for clinical applications aiming at a non-invasive, real-time, *in-situ* dose verification. This conclusion is based on the existing spatial correlation obtained between the depth-dose profile and the profile obtained with collimated photons by means of the single-pixel RTmon system tested experimentally in this work.

The single-pixel detector remained in each position for 25 s. In a full RTmon system the single-pixel scanning that provided the basis for this work would be unnecessary since a 2D detector such as the one shown in Fig. 2 (middle) would cover the entire field of view.

This study also shows that there are several challenges in implementing such a monitoring system in a realistic clinical environment, namely, a high background out-of-field photon flux, the need for heavy shielding and collimators, together with the typical poor spatial resolution of existing gamma-cameras constructed to operate in the relevant energy range of ~ 600 keV. Nevertheless, the single-pixel measurements presented in this work have dealt successfully with the aforementioned challenges, proving in a first step that the relevance of the results obtained substantiate the potential usefulness that can arise if a 2D RTmon system is constructed.

Acknowledgment

The authors acknowledge the support from the staff of milipeia – high performance computing cluster of the University of Coimbra (Pedro Almeida, Luís Pinto, and Prof. Pedro Vieira Alberto); from LIP (MSc. Rui Alves, Nuno Carolino, Eng. Nuno Dias, Joaquim Oliveira, Carlos Silva, Dr. Alberto Blanco, former Prof. Miguel Oliveira, João Silva, Prof. João Varela, MSc. Jorge Neves, Ricardo Caeiro, and Prof. Rui Ferreira Marques); from the Faculty of Medicine of the University of Seville (Bianey Palma and Prof. Sánchez-Doblado); from ISEC (Eng. João Pedro Alves, Mr. Cruz, and Paulo Brás); and from Mr. Sampaio for preliminary phantom fabrication.

References

[1] W. v. Elmpt, L. McDermott, S. Nijsten, M. Wendling, P. Lambin, and B. Mijnheer, "A literature review of electronic portal imaging for radiotherapy dosimetry," *Radiother. Oncol.*, vol. 88, no. 3, pp. 289–309, 2008.

[2] C. Thieke, U. Malsch, W. Schlegel, J. Debus, P. Huber, and R. Bendl *et al.*, "Kilovoltage CT using a linac-CT scanner combination," *Br. J. Radiol.*, vol. 79, pp. 79–86, 2006.
[3] M. Cunha, M. Pinto, H. Simões, B. Ferreira, M. C. Lopes, and P. Fonte *et al.*, "Dose-free monitoring of radiotherapy treatments with scattered photons: Concept and simulation study," *IEEE Trans. Nucl. Sci.*, vol. 60, no. 4, Aug. 2013.
[4] M. Bucci, A. Bevan, and M. Roach, III, "Advances in radiation therapy: conventional to 3D, to IMRT, to 4D, and beyond," *CA Cancer J. Clin.*, vol. 55, pp. 117–134, 2005.
[5] F. Sterzing, R. Engenhart-Cabillic, M. Flentje, and J. Debus, "Options of image-guided radiotherapy — a new dimension in radiation oncology," *Dtsch. Arztebl. Int.*, vol. 108, no. 16, pp. 274–80, 2011.
[6] J. Denham and M. Hauer-Jensen, "The radiotherapeutic injury — a complex wound," *Radiother. Oncol.*, vol. 63, pp. 129–145, 2002.
[7] M. C. Battaglia, H. Simões, V. Bellini, E. Cisbani, M. C. Lopes, and P. Crespo, "Orthogonal ray imaging with megavoltage beams: simulated results with an anthropomorphic phantom," in *Proc. IEEE Nuclear Science Symp. and Medical Imaging Conf., Records*, Anaheim, CA, USA, Oct. 3, 2012, M22–6.
[8] S. Agostinelli, J. Allison, K. Amako, J. Apostolakis, H. Araujo, and P. Arce *et al.*, "Geant4: a simulation toolkit," *Nucl. Instrum. Methods Phys. Res. A*, vol. 506, no. 3, pp. 250–303, 2003.
[9] J. Allison, K. Amako, J. Apostolakis, H. Araujo, P. Dubois, and M. Asai *et al.*, "Geant4 developments and applications," *IEEE Trans. Nucl. Sci.*, vol. 53, no. 1, pp. 270–8, Feb. 2006.
[10] J. Eaton, GNU Octave Manual, Network Theory Limited, ISBN: 0–9541617-2–6, 2002.
[11] M. Taylor and T. Kron, "Consideration of the radiation dose delivered away from the treatment field to patients in radiotherapy," *Med. Phys.*, vol. 36, pp. 59–71, 2011.
[12] C. Reft, R. Runkel-Muller, and L. Myrianthopoulos, "In vivo and phantom measurements of the secondary photon and neutron doses for prostate patients undergoing 18 MV IMRT," *Med. Phys.*, vol. 33, pp. 3734–3742, 2006.
[13] D. Rogers, I. Kawrakow, J. Seuntjens, B. Walters, and E. Mainegra-Hing, NRC user codes for EGS NRC, NRCC Rep. PIRS–702 (revC), National Research Council of Canada, Ottawa, ON, Canada, 2011 [Online]. Available: http://irs.inms.nrc.ca/software/egsnrc/documentation.html
[14] F. Verhaegen and J. Seuntjens, "Monte Carlo modelling of external radiotherapy photons beams," *Phys. Med. Biol.*, vol. 48, pp. R107–R164, 2003.
[15] B. Bednarz and X. G. Xu, "Monte Carlo modeling of a 6 and 18 MV Varian clinac medical accelerator for in-field and out-of-field dose calculations: development and validation," *Phys. Med. Biol.*, vol. 54, pp. N43–N57, 2009.